Dalton Transactions

ROYAL SOCIETY OF CHEMISTRY

PAPER

View Article Online
View Journal | View Issue

Cite this: *Dalton Trans.*, 2022, **51**, 10787

Indium-modified copper nanocubes for syngas production by aqueous CO_2 electroreduction†

Alessandro Niorettini,[a] Raffaello Mazzaro,*[b,c] Fabiola Liscio,[c] Alessandro Kovtun,[d] Luca Pasquini,[b,c] Stefano Caramori[a] and Serena Berardi*[a]

Received 11th March 2022,
Accepted 29th April 2022

DOI: 10.1039/d2dt00779g

rsc.li/dalton

Electroreduction of carbon dioxide represents an appealing strategy to rethink a waste product as a valuable feedstock for the formation of value-added compounds. Among the metal electrodes able to catalyze such processes, copper plays a central role due to its rich chemistry. Strategies aimed at tuning Cu selectivity comprise nanostructuring and alloying/post-functionalization with heterometals. In this contribution, we report on straightforward electrochemical methods for the formation of nanostructured Cu–In interfaces. The latter were fully characterized and then used as cathodes for CO_2 electroreduction in aqueous environment, leading to the selective production of syngas, whose composition varies upon changing the applied bias and indium content. In particular, gaseous mixtures compatible with the synthesis of methanol or aldehydes (*i.e.* respectively with 1 : 2 and 1 : 1 CO/H_2 ratios) are produced at low (*i.e.* −0.62 V *vs.* RHE) applied bias with >3.5 mA cm^{-2} current densities (in absolute value). Even if the proposed cathodes undergo structural modifications upon prolonged exposure to CO_2 reduction conditions, their catalytic activity can be restored by introducing an additional In(III) precursor to the electrolytic solution.

1. Introduction

The level of CO_2 in the atmosphere is constantly growing mainly due to anthropogenic activities. The resulting greenhouse effect causes global warming, leading to the intensification of natural phenomena, such as hurricanes, floods and wildfires. Thus, it is pivotal to find solutions to mitigate the CO_2 net emissions urgently. Three strategies are currently under study, *i.e.* decarbonization, carbon sequestration and carbon recycling. The first strategy aims at the (eventual) complete elimination of CO_2 emissions due to human activities, 25% of which is caused by electricity generation.[1] Thus, decarbonization implies the use of alternative energy vectors (*e.g.* hydrogen fuel) and the production of electricity *via* the exploitation of renewable sources (through photovoltaics, wind turbines, *etc.*). However, it is still difficult to envisage a complete substitution of the current fossil fuel-based technologies involving several key industrial processes (such as the production of plastic, cement, ammonia, *etc.*) and transportation. On the other hand, the second strategy aims at preventing CO_2 release into the atmosphere. In this sense, carbon capture and storage (CCS) processes are implemented in order to separate the CO_2 produced in a plant and store it underground. Considering all, the third approach, *i.e.* carbon recycling, is the more promising (provided the use of electricity produced *via* renewable technologies) as CO_2 is converted to value-added products. It is worth noting that every recycling reaction is a reduction, with carbon being in its highest oxidation state in CO_2. The source of protons and electrons would be water in the most ideal case. Examples of CO_2 hydrogenation reactions, in which H_2 acts as the reductant, have also been proposed.[2] Alternatively, carbon dioxide reduction (from now on, CO_2R) can be performed by exploiting either (bio)catalysis[3] or electrochemistry.[1,4] With regard to the latter approach, it is interesting to note that several reduction products can be formed, depending on the catalyst and the reaction conditions (*e.g.* electrochemical set-up, electrolyte, *etc.*). When metallic catalysts are used, straightforward categorization is possible, taking into account the major reaction product.[5] In particular, (i) metals such as Au and Ag display the preferential formation of carbon monoxide; (ii) p-block elements (Sn, In, Pb, *etc.*) almost selectively convert CO_2 to formate ions; (iii) Fe, Ti, Ni,

[a]*Department of Chemical, Pharmaceutical and Agricultural Sciences, University of Ferrara, Via Luigi Borsari 46, 44121 Ferrara, Italy. E-mail: serena.berardi@unife.it; Tel: +39-0532-455368*
[b]*Department of Physics and Astronomy, University of Bologna, Via Berti Pichat 6/2, Bologna, Italy*
[c]*CNR-IMM, Via Piero Gobetti 101, Bologna, Italy*
[d]*CNR-ISOF, Via Piero Gobetti 101, Bologna, Italy*
† Electronic supplementary information (ESI) available. See DOI: https://doi.org/10.1039/d2dt00779g

and Co are inefficient CO_2R catalysts as they are mainly promoting hydrogen production from the competitive water reduction reaction; and (iv) Cu leads to products with a higher degree of reduction, as well as to multicarbon products. The unique role played by copper in this kind of chemistry is related to its peculiar values of the binding energy of key CO_2 reduction intermediates. In particular, Cu is the only metal that has a negative adsorption energy for *CO and a positive adsorption energy for *H (the asterisks indicate a site on the electrodic surface).[5] Extensive work was made to unveil the mechanistic aspects beyond this chemistry, being able to yield up to 16 different reduced products from the electrolysis of an aqueous buffered solution in the presence of bare copper foil.[6] At the same time, several studies were aimed at nanostructuring a Cu foil substrate (or at depositing preformed copper nanoparticles on inert substrates) in order to provide a catalytic surface with possible different reactivity and/or better selectivity.

One of the most investigated nanostructuring strategies is the controlled formation of Cu oxides, which then undergo re-reduction under CO_2R conditions. Several methods have been reported for the oxidation of Cu foil surfaces. For example, Kanan and coworkers reported a thermal treatment yielding rod-like nanostructures, with improved CO and formate selectivity at lower overpotentials with respect to a polycrystalline Cu foil.[7] The Roldan Cuenya group instead used an oxygen plasma treatment, resulting in the formation of nanocubic structures with high selectivity for ethylene, namely 62% maximum faradaic efficiency (FE) at −0.9 V *vs.* the reversible hydrogen electrode, RHE (unless otherwise stated, all the potential values in this paper are reported *vs.* RHE).[8] A similar cubic morphology was obtained by Nilsson and coworkers *via* successive oxidative–reductive cycles in the presence of templating chloride ions,[9] showing the same preferential formation of ethylene, starting from −0.6 V. The Roldan Cuenya group reported also on the optimization of plasma-induced treatment, leading to the fine tuning of the morphology, ion content and defect density of Cu nanocubes and resulting in the production of significant amounts of ethanol (22% FE at −1 V) together with ethylene (45% FE under these conditions).[10]

Even if the formation of hydrocarbons and alcohols *via* CO_2R represents the holy grail of this kind of chemistry, other reduction products have a potential industrial interest. Among them, carbon monoxide is an important building block in organic and organometallic synthesis, especially when produced in conjunction with hydrogen (the latter originating from the competitive water reduction reaction). Indeed, gaseous mixtures of CO and H_2 in appropriate ratios constitute the synthesis gas (syngas), which is employed in industrially relevant processes, such as the Fischer–Tropsch process. This reaction enables the production of liquid fuels (diesel and gasoline), olefins, methanol and methane, depending on the CO/H_2 ratio, as well as on the catalyst nature and reaction conditions.[11–13] As already mentioned, CO_2 is generally reduced to CO in the presence of noble metals, such as Au and Ag. However, Spurgeon and coworkers reported the selective formation of tunable ratios of syngas also using a Cu foil, providing a specific electrochemical pre-treatment.[14] In particular, they reported a pulsed-bias electrochemical reduction in the millisecond time regime, which results in morphological changes of the foil surface and, in turn, in a different stabilization of key intermediates, leading to the observed catalytic selectivity.

Alternative strategies aimed at tuning the CO_2R selectivity of bare Cu entail the formation of alloys. Indeed, several examples of mixing Cu with many other metals have been reported, resulting in either bulk or surface alloys, guest metal modified surfaces, or bimetallic core–shell structures.[1,15]

Inspired by these works, in this contribution we will report on straightforward electrochemical treatments aimed at nanostructuring Cu foils and further functionalizing them with indium, in order to yield both improved selectivity for syngas and high performance in terms of current density. The latter is an important, yet often overlooked, aspect in view of the possible commercialization of CO_2R devices. Indeed, commercial electrolyzers generally operate at 200 mA cm^{-2}, with >70% efficiency,[16] while the typically reported performances of CO_2R electrocatalysts are <3 mA cm^{-2}.

Literature examples of Cu–In nanostructured catalysts for CO_2R are still limited. For example, Takanabe and coworkers reported the electrochemical reduction of $CuInO_2$, resulting in the formation of $Cu_{11}In_9$ and Cu_7In_3 alloys, with high efficiency in CO and formate production (respectively 70% and 20% FE at −0.8 V).[17] The Züttel group reported on a Cu–In interface obtained when a thin layer of In was formed by dipping on top of $Cu(OH)_2$ nanowires.[18] When the In content is 20% *vs.* Cu, best performances in terms of CO evolution are observed, *i.e.* 93% FE at −0.6 V. Zangari and coworkers instead reported on the co-electrodeposition of mixed Cu–In phases with different compositional and dendritic morphologies.[19] The electrodes with 40 at% In showed high formate production (49% FE), together with syngas in the optimal ratio $H_2/CO = 2.6$, while the maximum amount of formate (62% FE) was obtained with 80 at% In cathodes. An array of Cu–In electrocatalyst coatings with good control of metal stoichiometries was prepared by the Berlinguette group *via* near-infrared driven decomposition of mixed-metal precursor solutions. Excellent selectivity for CO (*ca.* 90% FE) was maintained by Cu_xIn_{1-x} alloys, with x being in the range 0.5–0.8.[20]

Herein we report on the use of nanostructured indium-modified copper cathodes for the selective formation of syngas *via* CO_2 electroreduction in aqueous medium. The syngas composition can be tuned by varying the indium content and/or the applied potential. In particular, under −0.62 V applied bias, we obtained 1 : 2 and 1 : 1 CO/H_2 mixtures, which can be exploited for the synthesis of methanol and hydroformylation reactions, respectively. Even if the medium-term operation under CO_2R conditions results in some structural modifications of our cathodes, their performances can be fully restored upon the addition of an In(III) precursor to the electrolytic solution.

2. Experimental

2.1. Materials

Copper foil (0.127 mm thick, 99.9% metal basis), titanium foil (0.25 mm thick, 99.5% metal basis), a Nafion® N-117 membrane (0.180 mm thick), $KHCO_3$ (99.7–100.5%), and K_2SO_4 (99%) were purchased from Alfa Aesar. Indium foil (0.1 mm thick, 99.995%) was purchased from MaTeck. CO_2 (>99.9%) was purchased from the SOL group. CO (99.0+%), indium(III) nitrate hydrate (99.999%), dimethylformamide (≥99.8%), and deuterium oxide (99.9 atom. % D) were purchased from Sigma-Aldrich. Citric acid (anhydrous, >99.5%), KCl (99.5%) and H_3PO_4 (85%) were respectively purchased from Fluka, Carlo Erba and VWR Chemicals. Unless otherwise stated, all chemicals were used without further purification. All electrolytic solutions were prepared using reagent grade water (Millipore, 18 MΩ resistivity).

2.2. Preparation of the cathodes

Before use, Cu foils were electropolished in 85% H_3PO_4, holding +4 V voltage *vs.* a titanium counter electrode for 300 s. After this treatment, some foils were subjected to pulsed anodization, aimed at nanostructuring the surface. Briefly, the electropolished Cu foil was placed horizontally in a single compartment, three-electrode cell and then immersed in a 0.1 M K_2SO_4/0.04 M KCl aqueous electrolyte. The soldered ohmic contact was fully protected with epoxy resin. An Amel 552 potentiostat coupled with an Amel 568 in-line function generator was used to apply a square wave (SW) anodization, switching between +1 V and 0 V (*vs.* a double-jacketed SCE) with a frequency of 10^3 Hz for a total time of 300 s. The resulting electrode was later reduced in a 0.5 M aqueous $KHCO_3$ solution *via* 20 successive linear voltammetry scans, sweeping the applied potential in the range of −0.2/−1.5 V *vs.* SCE at a scan rate of 20 mV s^{-1}. This procedure allows for the reduction of the oxidized Cu layer resulting from the anodization, leading to the formation of the actual catalytic interface called OD-Cu (for oxide-derived Cu) throughout the text.

Indium was electrodeposited on OD-Cu electrodes in a two-electrode cell configuration, using an indium wire as the counter electrode, following a slightly modified literature procedure.[21] The deposition was carried out in the galvanostatic mode, while stirring a solution containing 0.04 M indium(III) nitrate and 0.5 M citric acid. The process was carried out until charge densities of 18, 36 and 54 C cm^{-2} were transferred, respectively, yielding OD-Cu_In18, OD-Cu_In36 and OD-Cu_In54 cathodes.

2.3. Morphological and structural characterization

Morphological characterization was performed using a Zeiss Leo 1530 Field Emission Scanning Electron Microscope (FE-SEM), operated at 5 kV. Nanoscale structural and compositional analyses were carried out by using a Philips TECNAI F20 ST high resolution transmission electron microscope (HR-TEM) operating at 200 kV. The instrument is equipped with an energy dispersive micro-analysis (EDS) and scanning transmission high angle annular dark field (STEM-HAADF) detector. For TEM observations, the cathode surface was scratched and the powder sonicated in isopropanol for 5 minutes, before being dropcast onto holey carbon-coated Au grids. The samples were dried at room temperature before observation.

X-Ray Diffraction (XRD) patterns were recorded using a Rigaku SmartLab diffractometer equipped with a Cu-rotating anode and Soller slits to obtain a parallel beam with a divergence of 0.1°. Measurements were performed in specular and Grazing Incidence (GI) geometries to probe films at different penetration depths, from a few nanometers to microns. Due to the high film roughness, the incident angle in GI-XRD scans was varied from 0.5° to 3° in order to detect Bragg peaks from the film surface. Therefore, the exact values of the penetration length could not be estimated.

X-ray photoelectron spectra (XPS) were recorded using Mg K_α excitation and analysed using a hemispherical analyser (Phoibos 100, Specs). The survey and high-resolution spectra were acquired with energy resolutions of 1.4 eV and 0.9 eV, respectively, on freshly sputtered silver (Ag 3d). A spectrometer was calibrated to the Au $4f_{7/2}$ peak at 84.0 eV. Conductive carbon tape was used to fix and electrically ground the sample. No electrostatic charging effects were observed. The spectra were fit using the CasaXPS software after Shirley's background subtraction.

2.4. Electrochemical characterization

2.4.1 Electrolyte purification. The presence of metal cation impurities (especially Fe^{2+}, Pb^{2+} and Zn^{2+}) in electrolytic solutions used for CO_2 electroreduction is known to cause co-deposition of the corresponding metals on the cathodic surface, possibly leading to modification of the catalytic properties.[22] Although nanostructured electrodes should be less sensitive to this process,[23] the electrolytic solution was pre-electrolyzed using two titanium foils held at −2 V for 15 h under nitrogen bubbling.[24] ICP-mass analysis was then performed, confirming the absence of Fe^{2+}, Pb^{2+} and Zn^{2+} within the limits of technique sensitivity (<0.5 ppm).

2.4.2 Product accumulation and analysis. CO_2 reduction experiments were carried out in a two-compartment, custom-made polymethylmethacrylate cell. The cathodic side hosts both the working (Cu-based cathode) and reference (SCE) electrodes, while the anodic one contains the Pt counter electrode. The two compartments are separated using a Nafion® 117 membrane. Both the anolyte and the catholyte consisted of a 0.5 M $KHCO_3$ aqueous solution saturated with CO_2 (resulting pH = 7.4) and pre-electrolyzed according to the abovementioned procedure. The working electrodes were soldered to Cu wires and then isolated from contact with the electrolyte by using epoxy resin. Pulsed electrolyses were performed in order to accumulate the reduction products (conditions described in the main text). Unless otherwise stated, all the potential values are reported

versus the reversible hydrogen electrode (RHE), calculated using the formula:

$$V\ (vs.\ \mathrm{RHE}) = V\ (vs.\ \mathrm{SCE}) + 0.24 + 0.059 \cdot \mathrm{pH}.$$

The cathodic compartment of the cell was connected to a headspace, from which gaseous samples were automatically collected. Their detection and quantification were performed using an Agilent 490 micro GC (Agilent Technologies) equipped with a 5 Å molecular sieve column (10 m) and a thermal conductivity detector, with Ar as the carrier gas. Quantification of formate was performed *via* ^{1}H-NMR spectroscopy (Agilent, 300 MHz), using DMF as the external standard and a customized water suppression sequence. For each product, the faradaic efficiency (FE) was calculated as:

$$\mathrm{FE} = \frac{n \cdot F \cdot \mathrm{mol}}{Q_{\mathrm{tot}}}\%$$

where mol is the quantified amount of product, n is the number of electrons involved in the specific reduction reaction; F is the Faraday constant; and Q_{tot} is the total amount of charge passed at the interface during the pulsed bulk electrolysis experiments.

2.4.3 Determination of electrochemical surface area (ECSA) by double layer capacitance measurements. Experiments were carried out using an Autolab PGSTAT30 potentiostat in a 3-electrode set-up using a Pt wire as the counter electrode and a saturated calomel electrode (SCE) solution as the reference in 0.5 M aqueous $KHCO_3$. CV scans were recorded at scan rates of 5–200 mV s^{-1}, in a potential range at which no faradaic processes occur. From the resulting traces, the capacitive current was calculated as $(j_a - j_c)/2$, with j_a and j_c being the anodic and cathodic current densities normalized by the geometric area of the electrodes, respectively. When the resulting values were plotted *vs.* the scan rate, the slope corresponds to the electrode capacitance. The roughness factor (RF) of the nanostructured electrodes was then calculated, attributing RF = 1 to Cu foil (assumed to be featureless).

3. Results and discussion

3.1. Structural and morphological characterization of the samples

The synthesis of Cu nanostructures was realized by applying a fast (10^3 Hz) square wave anodization method to an electropolished Cu foil in the presence of chloride ions. The latter are known to act as templates for the formation of cubic Cu structures with a (100) facet orientation.[25,26] It was reported that for nanostructuring protocols involving oxidative steps (*e.g.* either thermal,[7] electrochemical[9,14] or plasma-induced[8,10]), a Cu_2O phase is firstly produced, which then undergoes reduction during the first steps of CO_2R. The Roldan Cuenya group recently documented this process under *in operando* conditions, using liquid cell transmission electron microscopy.[27] They also evidenced that some dynamical changes in the cubic morphology can occur, resulting in the formation of Cu dendritic structures.[27]

Fig. 1 resumes the morphological and structural characterization of the nanostructured Cu cathodes after pulsed anodization modification. Fig. 1(a and b) report the SEM images of an OD-Cu sample, showing that this nanostructuring approach results in the deposition of randomly oriented nanocubes with an average size of <1 μm, even if some larger nanocubes are also observed. In the background of the SEM images, dendritic structures were also noticed, as previously discussed.

The crystal phase of the nanocubes was investigated by X-ray diffraction. Fig. 2a shows a comparison of the XRD patterns collected on bare OD-Cu in specular and grazing incidence geometries, which probe a thickness of a few μm and a few nm, respectively. The specular scan shows Bragg peaks of metallic face-centered cubic Cu with a partial preferred orientation along the 200 direction and Bragg reflections of the Cuprite (Cu_2O) crystal structure. At grazing incidence, the (111)Cu/(200)Cu intensity peak ratio reflects the polycrystalline nature of the surface. The results indicate that the 200 texturing originates from the underlying Cu foil, while the Cu and Cu_2O nanostructures grown on the top of it are randomly oriented, or, at least, polycrystalline.

HR-TEM characterization of the OD-Cu nanocubes also confirms that metallic Cu and cuprite phases are concurrent in the sample (Fig. 1c–e), probably due to the formation of a native oxide layer upon atmosphere exposition. EDS analysis of the sample further proves the presence of an oxide layer on the nanocubes (Fig. 1f), while the complete structural characterization of their core is prevented by their thickness, fully electron-opaque.

The enhancement of the electrochemical surface area (ECSA) resulting from surface nanostructuring was measured *via* cyclic voltammetry experiments (see Fig. S1†). By determining the capacitive current with respect to the bare Cu foil, taken as the standard, we were able to estimate the roughness factor (RF) of the OD-Cu cathodes, which resulted to be *ca.* 50 (see Table S1†).

Fig. 3 shows the SEM images of In-modified cathodes, displaying a finer texturing and enhanced roughness of the nanocube surface that suggests the presence of an additional coating layer. However, the background areas behind the nanocubes appear smoother than in OD-Cu cathodes without indium, particularly for longer deposition times.

This results in a lower ECSA with respect to the OD-Cu cathodes, as evidenced in Fig. S1e–j and Table S1.† Indeed, the OD-Cu_In18, OD-Cu_In36 and OD-Cu_In54 electrodes respectively displayed a roughness factor of 22, 27 and 39.

With regard to XRD characterization (Fig. 2b), the specular XRD pattern of OD-Cu_In54 shows Bragg peaks of metallic Cu with the preferential 200 orientation. As already noted for In-free cathodes, the GI-XRD measurements highlight a lower degree of preferential orientation of Cu crystallites, confirming that the produced nanostructures are not epitaxial with respect to the original Cu foil. The Bragg reflections of Cu_2O were not detected in the In-modified cathode, indicating that the

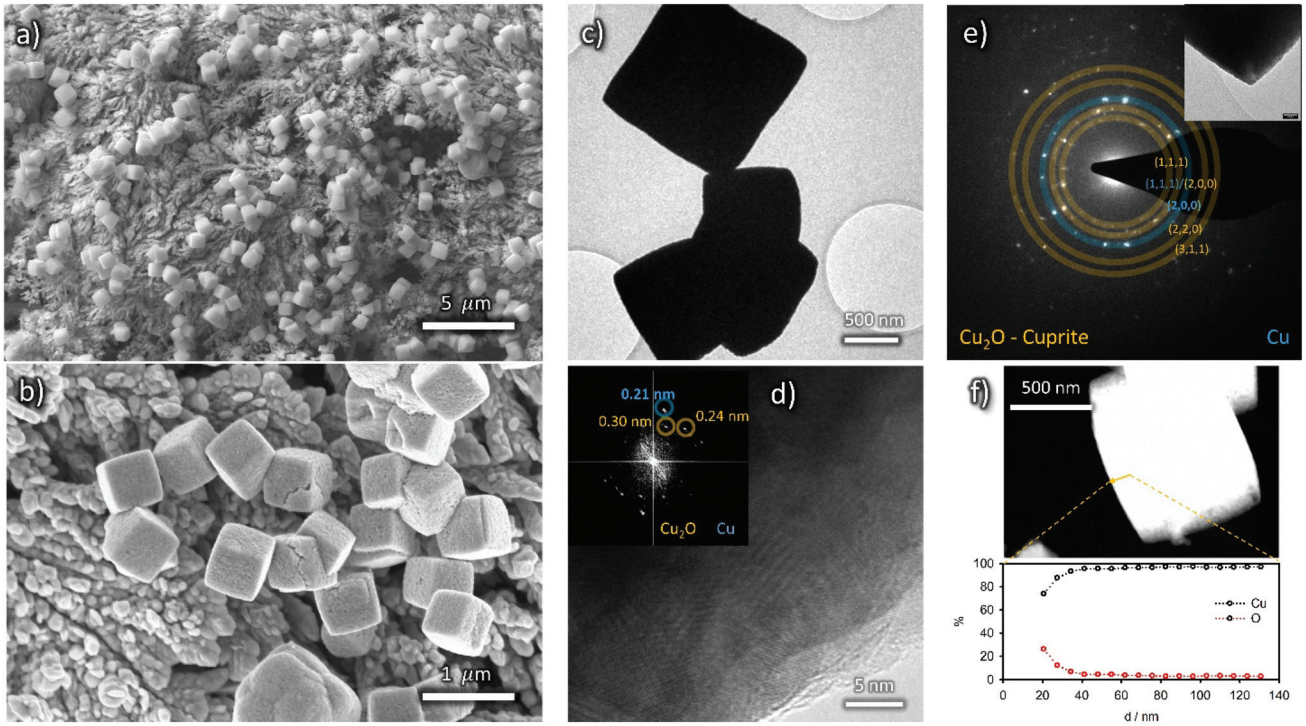

Fig. 1 (a and b) FE-SEM images of bare OD-Cu; (c) low magnification and (d) HR-TEM micrographs of OD-Cu nanocubes displaying reflections compatible with Cu_2O and the Cu lattice (FFT in figure d inset); (e) selected area electron diffraction (SAED) of a single nanocube (inset) highlighting concurrent cuprite and metallic Cu phases; (f) STEM-HAADF micrograph of a single cube and Cu/O content obtained by EDS analysis along the highlighted profile.

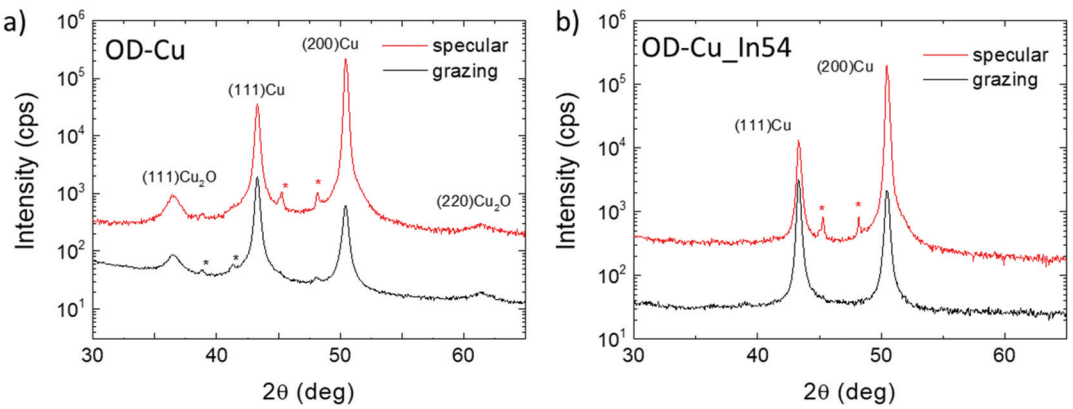

Fig. 2 Specular- and GI-XRD scans on bare OD-Cu (a) and OD-Cu_In54 (b). Stars indicate peaks coming from spurious wavelengths.

indium containing coating protects the underlying Cu from oxidation. No other Bragg reflections were detected, suggesting that the In-containing phases diffract very weakly, probably because of poor crystallinity.

The morphology of the nanocubes may be still recognized in the low magnification TEM micrographs (Fig. 4a) but the HR-TEM image reveals the presence of a beam-sensitive amorphous layer around the nanocubes with embedded crystalline nanoparticles (<5 nm diameter, Fig. 4b and c). The *d*-spacing is compatible with both In_2O_3 and $In(OH)_3$; an assignment will be done later in the text, based on XPS analysis. Consistently, EDS mapping displays that the described coating layer is rich in In and O (Fig. 4d).

In order to gain more insights into the cathodes' surface composition, their characterization *via* XPS was also performed. XPS Cu 2p, O 1s, C 1s and K 2p core level transitions were found in the XPS survey signal of OD-Cu (Fig. 5a). From the high resolution spectra of Cu 2p (Fig. 5b) and the corresponding Auger transition of Cu LMM (Fig. 5a), the chemical state of Cu in OD-Cu was identified; the values of the Cu $2p_{3/2}$

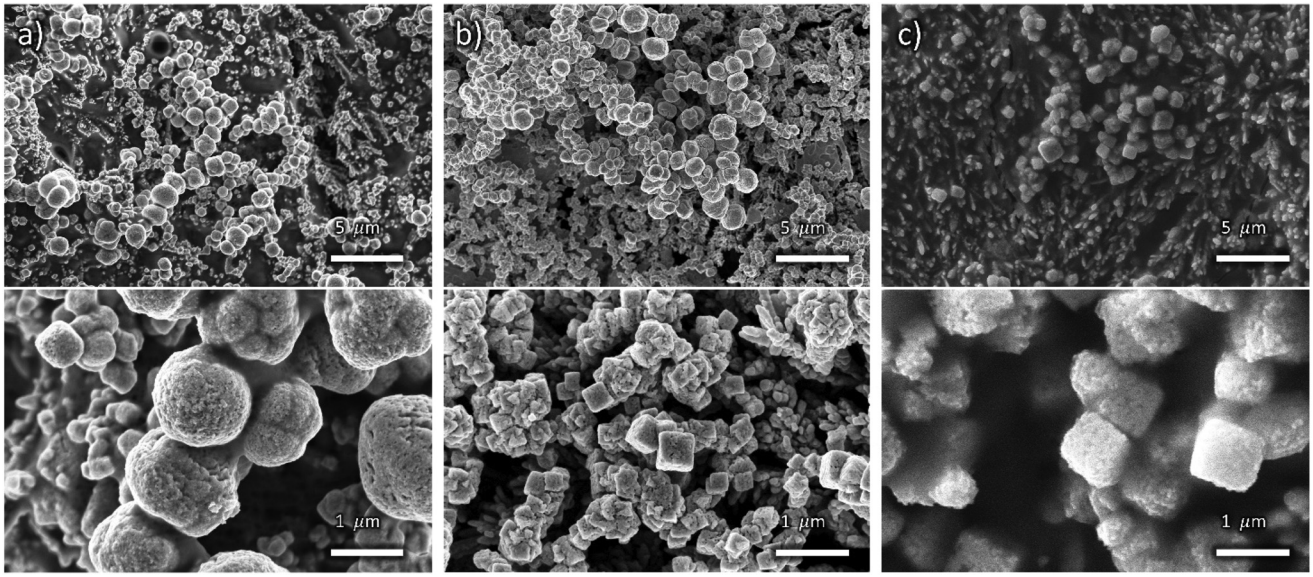

Fig. 3 Low (top) and high (bottom) magnification FE-SEM images of OD-Cu_In18 (a), OD-Cu_In36 (b) and OD-Cu_In54 (c).

binding energy (932.5 ± 0.1 eV) and the Auger modified parameter (AP = 1849.1 ± 0.2) were in agreement with Cu(I) in oxidized form (Cu_2O);[28] nevertheless, the presence of Cu(II) components was below 10%, as deduced from the Cu 2p fit in Fig. 5b. The presence of Cu_2O was further supported by the presence of an O–Cu signal in O 1s at 530.6 eV (Fig. S2a†).[29,30] From the high resolution C 1s signal, apart from aliphatic/adventitious carbon at 285.3 eV, the presence of a carboxyl group or carbonate ions associated with the peak at 289 eV can be observed (Fig. S2b†). In the same C 1s region, the K 2p signal was found. Both these features are due to adsorbed ions, residual from the OD-Cu synthesis.

After In deposition, the signal of In $3d_{5/2}$ at 445.2 eV has revealed the presence of In(III) in OD-Cu_In36 (Fig. 5e).[31] One may conclude that the most probable chemical state could be In_2O_3, but considering that In_2O_3 usually presents a slightly lower chemical shift ($3d_{5/2}$ 444.7 eV), this association is not obvious. A recent paper by Detweiler[32] reports a systematic study of In oxidation under dry and wet conditions, finding a reliable energy separation between In_2O_3 (444.7 eV) and $In(OH)_3$ (445.1 eV), compatible with our results. Thus, it is reasonable to claim that the chemical state of In in OD-Cu_In36 is $In(OH)_3$. The increase in the O 1s signal supported both the formation of In_2O_3 or $In(OH)_3$, notwithstanding, the signal of O–In is in the same region of O–Cu, being 530.3 eV and 530.7 eV, respectively, but no significant increase was found; while the hydroxyl In-OH signal at 532 eV has contributed to the main peak of O 1s (Fig. S2c†), together with oxygen in the carbonate.[33]

After the galvanostatic deposition of indium, the K 2p signal disappeared and the Cu chemical state changed (Fig. 5d) from Cu(I) to Cu(II), as confirmed by the binding energy of Cu $2p_{3/2}$ (934.4 ± 0.1 eV) and AP (1850.2 ± 0.2 eV). From the Cu 2p fit in Fig. 5d, at least 3 components were found: Cu_2O, CuO and $Cu(OH)_2$. The accurate ratio of Cu(II) was hard to find. Cu(II) is not stable under X-ray irradiation and the evolution of the Cu 2p signal in OD-Cu_In36 (Fig. S3a†) revealed the photoreduction phenomenon that usually occurs under similar conditions.[34,35] Thus, Cu(II) was certainly the most abundant prior to the irradiation, while the presence of Cu(I) is mainly ascribed to X-ray irradiation. The O 1s signal of $Cu(OH)_2$ was found in the 532 eV region, the same region of indium hydroxide (see Fig. S2c†).

In summary, XRD showed that the deposition of an In layer prevented the formation of a relatively thick (*e.g.*, detectable by XRD) Cu_2O layer. However, XPS shows that the Cu oxidation state in the near surface layers changes from the prevalently Cu(I) of Cu_2O to the dominant Cu(II) of CuO and $Cu(OH)_2$ as a consequence of In deposition. Indium itself occurs as oxidized In(III) in $In(OH)_3$.

3.2. CO_2R activity

The cathodes were tested under electrochemical CO_2R conditions in a two-compartment, three-electrode electrochemical cell in 0.5 M $KHCO_3$ saturated with CO_2. Fig. 6 shows the current density normalized for the geometrical area (*j*) *vs.* the applied bias (*V*) curves for all the samples. As expected, the output current generated with the nanostructured OD-Cu electrode is higher (*ca.* 5-fold) than that registered with the Cu foil, reaching up to −53 mA cm^{-2} at −0.92 V.

The different performances of these two interfaces are also evident from the quantitative analysis of the CO_2R products, reported in Fig. S4a and b† in terms of faradaic efficiency (FE) in the range −0.62 V/−0.92 V. It is worth noting that the reductive working potential indicated is applied for 4 cycles of 300 s each, spaced by short (40 s) reconditioning steps at the open circuit potential (see *e.g.* Fig. S5a† for the curves obtained for an OD-Cu_In36 cathode). This procedure was introduced in

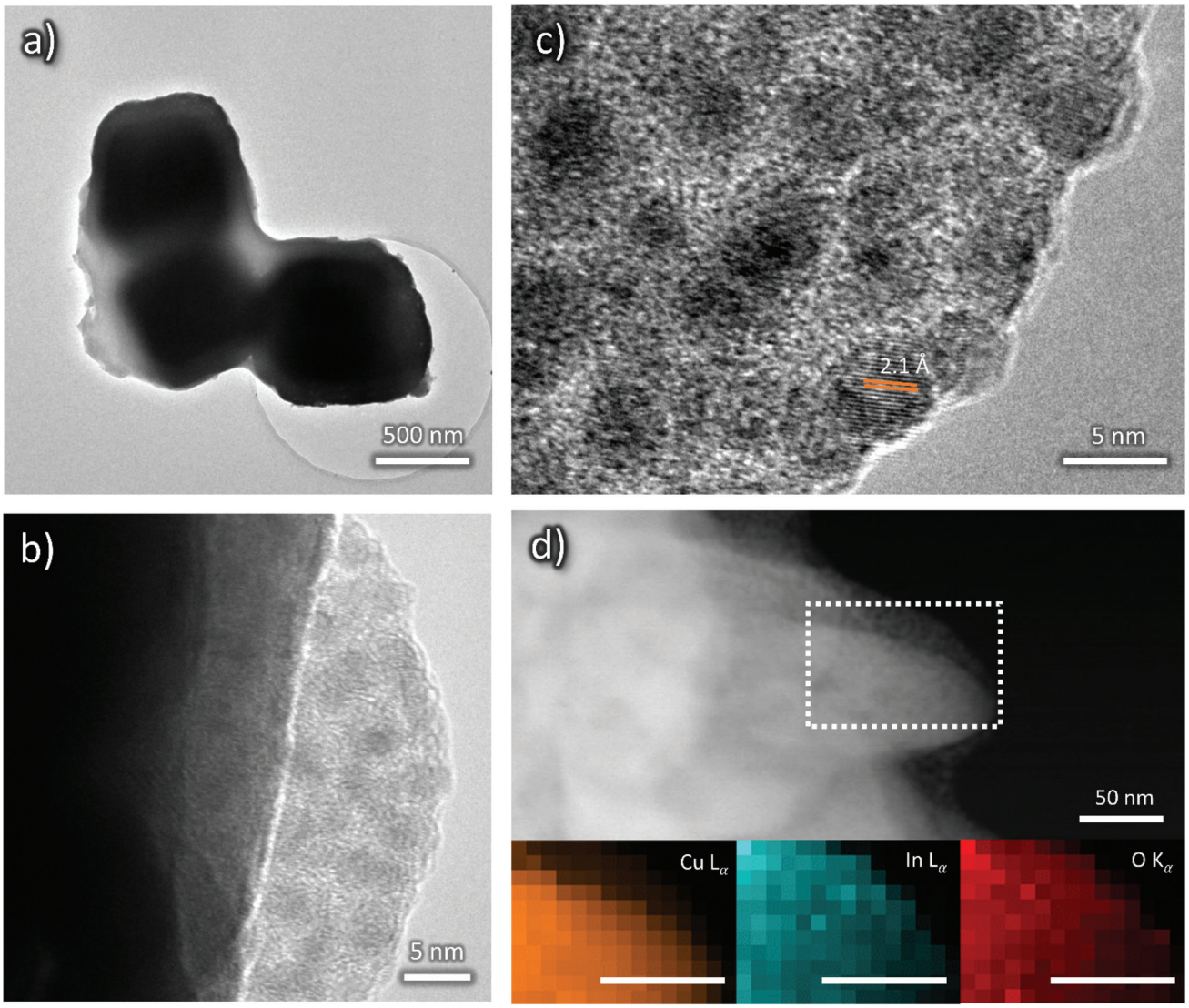

Fig. 4 (a) Low magnification TEM and (b and c) HR-TEM micrographs of the OD-Cu_In18 sample. The coating layer around the Cu nanocubes embeds the crystalline nanoparticles, the *d*-spacing of which is compatible with that of In_2O_3 or $In(OH)_3$. (d) STEM-HAADF micrograph of an OD-Cu_In18 nanocube surface feature and related EDS mapping displaying higher concentrations of In and O in the coating layer.

order to remove adsorbed poisoning species, likely graphitic carbon deposits[36] and/or the produced CO itself.[37–39] Anyway, the reconditioning steps only impact the total electrolysis time by less than 10%. At the same time, pulsed CO_2 electroreduction conditions were reported to cause transient changes in local pH and CO_2 concentrations,[40] as well as in the electric field near the catalyst surface.[14] This behavior can significantly impact the binding energies of the adsorbed reaction intermediates, which in turn affect the product distribution. Indeed, with regard to the activity of the Cu foil, we observe FE values that differ from those generally reported.[1,6] In particular, CO evolution starts at −0.62 V, peaks at −0.72 V (max FE = 6%), and then decreases, while an appreciable production of formate and methane begins at −0.82 V (see Fig. S4a†). Anyway, the total CO_2R products account for *ca.* 10% of the total current, with H_2 being the main product (FE >46%). On the other hand, the OD-Cu cathodes display higher selectivity for CO, reaching up to 18% FE at −0.82 V, while formate starts to be produced at −0.62 V with a maximum FE of 8% (see Fig. S4b†). At −0.82 V applied bias, these cathodes also produce methane (with max FE = 3.5%) and ethylene (max FE = 5% at −0.92 V). Even if the total FE due to CO_2R is higher (*ca.* 25%) with respect to that of the Cu foil, the main product is still H_2.

Indium deposition greatly affects the performances of the mixed-metal cathodes. With regard to the current output (see Fig. 6), the Cu–In cathodes display decreased values at −0.92 V with respect to OD-Cu, which can be ascribed (at least partly) to reduced RF. Furthermore, we do not observe a linear dependence of the current density on the In content, with the order being OD-Cu_In36 < OD-Cu_In18 < OD-Cu_In54. Anyway, the selectivity of these composite interfaces towards syngas pro-

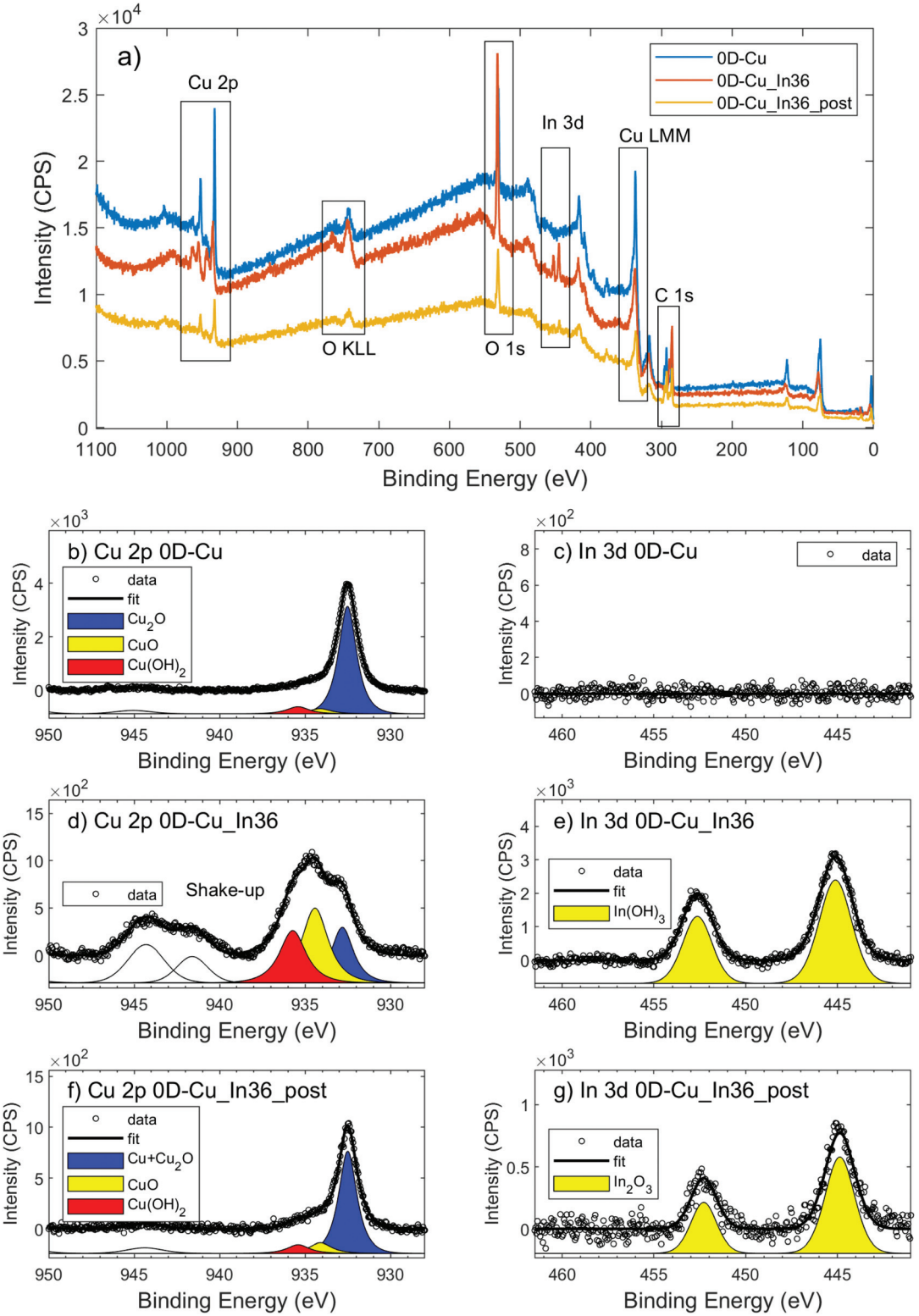

Fig. 5 (a) Survey XPS spectra of OD-Cu (blue), OD-Cu_In36 (red) and OD-Cu_In36_post (orange). XPS signals of Cu 2p, O 1s, In 3d, C 1s and K 2p are present, with Auger signals of O KLL and Cu LMM; (b-d-f) high resolution spectra of Cu $2p_{3/2}$ in OD-Cu (b), OD-Cu_In36 (d) and OD-Cu_In36_post (f); (c-e-h) high resolution spectra of In 3d in OD-Cu (c), OD-Cu_In36 (e) and OD-Cu_In36_post (g).

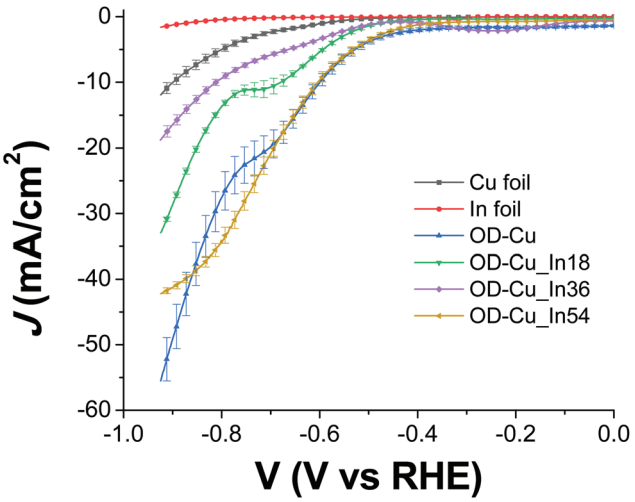

Fig. 6 *J*–*V* characteristics for the tested cathodes, recorded in 0.5 M $KHCO_3$ saturated with CO_2 (pH 7.4), normalized for the geometric area and corrected for the iR drop. The stable response of at least three electrodes has been averaged, and the corresponding curves are reported, together with the error bars.

duction significantly increases with respect to OD-Cu. Indeed, as evidenced in Fig. 7a and b, for OD-Cu_In18 and OD-Cu_In36, no other product than syngas is present in the explored bias range. Appreciable syngas evolution starts at −0.62 V, a relatively low overpotential for the production of the two gases. Under these conditions, the H_2/CO ratio is ≈2 : 1 for OD-Cu_In18 with *ca.* −5 mA cm^{-2} current density (see Fig. S5b†) and ≈1 : 1 with *ca.* −3.5 mA cm^{-2} for OD-Cu_In36 (Fig. S5a†). These syngas compositions are respectively compatible with the production of methanol[41] and with hydroformylation reactions.[42] A gaseous mixture with a H_2/CO ratio of ≈1 : 1 was also obtained for OD-Cu_In18 at −0.82 V, sustaining significant current densities in the range −15/−18 mA cm^{-2} (Fig. S5b†).

As far as the production of sole CO *versus* the applied bias is concerned, a typical volcano trend is observed, with the efficiency peaking at −0.72 V for both cathodes, and OD-Cu_In36 yielding a maximum FE of 80%. We also observed the dependence of the FE for CO production on the amount of deposited indium, with OD-Cu_In36 again being the optimized electrode that outperforms the other cathodes in all the explored potential range (see Fig. 6c). A qualitative comparison between the performances of our OD-Cu_In36 cathode and other Cu–In based interfaces reported in the literature is also provided in Table S3.†

At the same time, when the indium content increases, H_2 evolution becomes the dominant reaction (see Fig. S4c†), with the FE for CO production being <10% for OD-Cu_In54. A similar trend for CO and H_2 production was also observed by Züttel and coworkers for the surface modification of $Cu(OH)_2$ nanowires with metallic In nanoparticles.[18] Density functional theory studies revealed that the optimized bimetallic interfaces (*i.e.* those with the highest number of Cu–In interfacial sites,

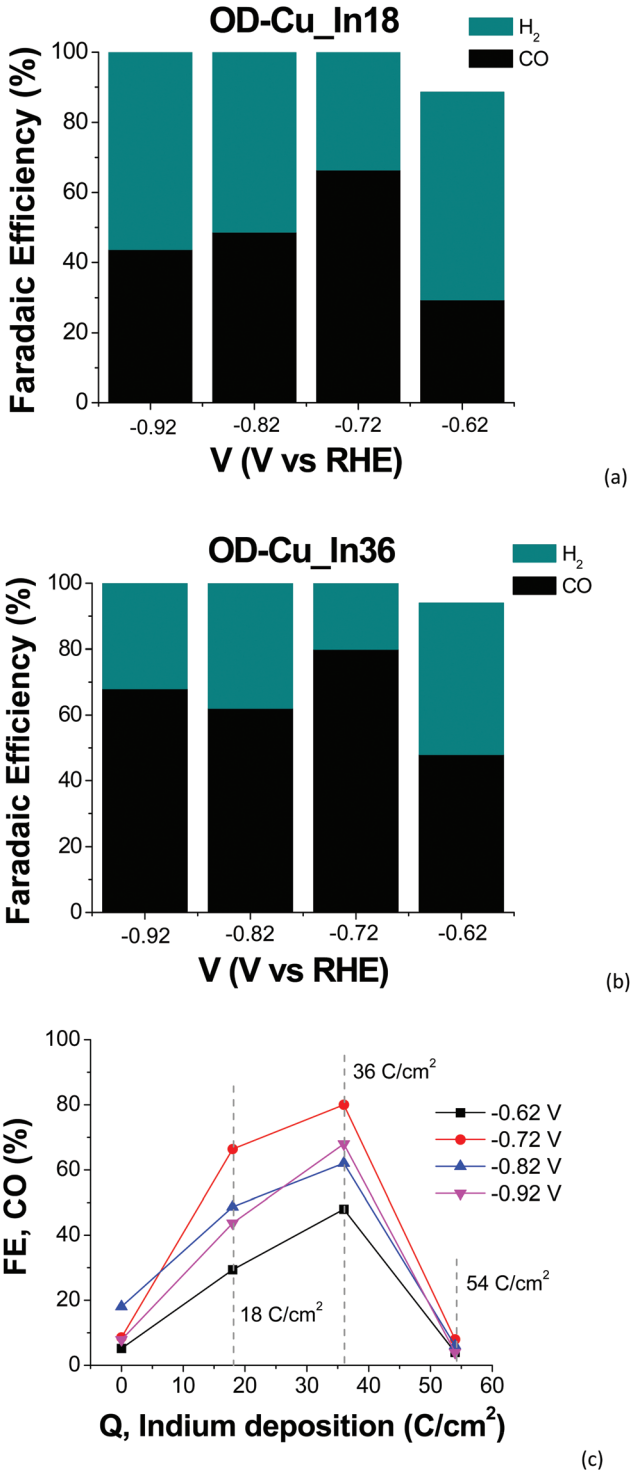

Fig. 7 (a and b) Faradaic efficiencies of the different products obtained with (a) OD-Cu_In18 and (b) OD-Cu_In36 cathodes as a function of the applied bias. Each bar is an average of at least three measurements. (c) Faradaic efficiency for CO production of the Cu–In cathodes as a function of the deposited indium.

generated by a medium coverage of In on the Cu surface) significantly decrease the free energy barrier for the formation of *COOH (the key intermediate for CO formation) and the

strength of the adsorbed *H (thus limiting H_2 production). Also in our case, when the deposited indium exceeds the optimal amount obtained for the OD-Cu_In36 cathode, the interfacial reactivity changes, closely resembling the catalytic outcomes obtained when using a bare In foil (see Fig. S4d†). Indeed, under our conditions, both the latter and the OD-Cu_In54 electrode produce only H_2 and CO in the low applied bias range, but at higher negative bias values formate ions are also produced (up to 19% FE at −0.92 V for OD-Cu_In54, see Fig. S4c†). These results further point out that pulsed electrolysis strongly affects the reactivity of the catalytic metal and the absorption/desorption of key intermediates as CO_2R by indium generally yields $HCOO^-$ as the main product.[1]

The observed enhanced selectivity for CO_2 reduction to CO can be due also to a synergistic effect between Cu and $In(OH)_3$, as recently pointed out by Larrazábal *et al.*[43] Indeed, when the $In(OH)_3$ layer was etched from an OD-Cu_In36 cathode by means of an acid treatment reported in the literature,[43] the CO_2R performances of the cathode were strongly reduced. As evidenced in Fig. S5c,† when comparing the FE for CO production by a pristine OD-Cu_In36 cathode with those of the exact same electrode after 2 successive etching treatments, under the latter conditions we formed *ca.* 2/3 and 1/3 of the initial CO amount.

While the chronoamperometric experiments for product detection and accumulation gave us the first hint of the good stability of our cathodes in a 20 min timescale, a representative OD-CuIn36 cathode was also tested under longer-term CO_2R conditions. Indeed, Fig. 8 shows the >2 hour-long electrolysis at −0.72 V, displaying that after the first 0.25 h, the current density sets at a quite stable value of *ca.* −3.5 mA cm^{-2}. However, when sampling the reaction, we observed a decrease in the initial CO amount (accounting for a 70% FE, the sole other product being H_2) down to *ca.* 10% FE after 1 h. With the performances in terms of current density essentially unvaried in this time frame, some structural modifications in the catalyst should occur, favoring H_2 evolution. In order to shed light on this behavior, we performed microscopic and spectroscopic characterization of the cathodes after the operation.

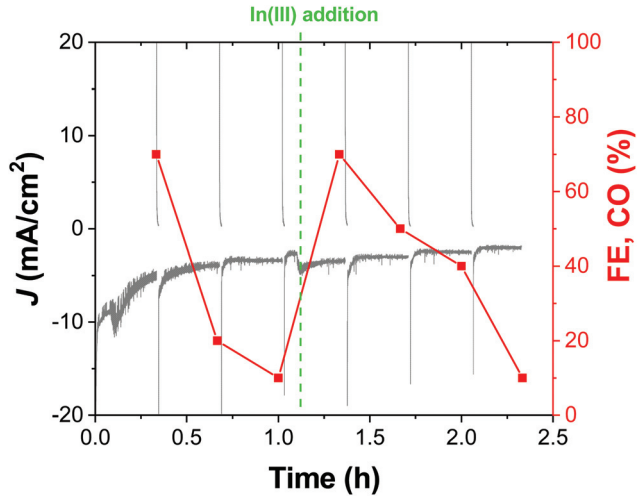

Fig. 8 Chronoamperometric trace of the OD-Cu_In36 cathode stepped between −0.72 V and the open circuit potential, OCP. The faradaic efficiency for CO production at different sampling times is also reported. The green dashed line marks the addition of 1 mL of a 0.04 M solution of $In(NO_3)_3$ in 0.5 M citric acid, aimed at restoring the active In-based layer and consequently the previous CO production.

In particular, XPS analysis evidenced that after 1 hour of electrochemical CO_2R the OD-Cu_In36 cathode (called OD-Cu_In36_post) presents the same elements of the pristine one (except for the appearance of K), but in the overall reduced chemical state: Cu is reduced from Cu(II) to Cu(I) + Cu(0) and In changes from the hydroxide to the oxide chemical state. Combining information from the main signal of Cu $2p_{3/2}$ (932.5 ± 0.1 eV) and the double signal present in the Auger Cu LMM signal (AP 1851.1 ± 0.2 eV for Cu(0) and AP 1849.1 ± 0.2 eV for Cu(I)), we can support that the surface after the electrochemical test is mostly a mix of metallic Cu and Cu_2O, pointing out that the XPS was performed *ex situ*, thus Cu_2O may also arise from the atmospheric passivation of metallic Cu. On the other hand, indium decreases at relative concentrations, from 1.8 to 0.8%, and presents a shift (see Fig. S3c†) in the binding energy from 445.2 eV to 444.9 eV compatible with the chemical change from the hydroxide to the oxide state, as discussed above. Finally, the O 1s signal presents an increase of pure oxide (Cu_2O and In_2O_3) components in the 530.8–530.5 eV region with respect to hydroxides and C–O at 532 eV.

Grazing-incidence XRD supports these results, evidencing the appearance of the cuprite phase after CO_2R, as also confirmed by an increase in the oxygen content in EDS analysis (see Fig. S6†). A lower indium content is also observed, probably due to a partial dissolution of the deposited In-based nanostructures, consistent with the drop in the FE for CO production observed over prolonged exposure to the electrolysis conditions. In agreement with that, the SEM and TEM micrographs do not exhibit a homogeneous distribution of the In-based coating, in contrast to what was observed before the electrolysis experiment (Fig. S7†).

However, the catalytic activity can be fully restored by performing an additional indium deposition step *in situ*. Indeed, as evidenced in Fig. 8, after the addition of $In(NO_3)_3$ to the electrolytic solution, the CO production was fully restored, in favor of the restoration of the active In-based layer.

4. Conclusions

Nanostructured Cu cathodes with a predominant nanocubic morphology were prepared *via* straightforward and readily available electrochemical procedures. Their characterization revealed the presence of both metallic Cu and Cuprite (Cu_2O). Further functionalization of these cathodes through In deposition led to the formation of heterointerfaces with enhanced activity towards the selective reduction of the greenhouse gas CO_2 to a valuable product, *i.e.* syngas. In particular, in aqueous solution and under low applied bias (*i.e.* −0.62 V), the

OD-Cu_In18 and OD-Cu_In36 cathodes produced gaseous mixtures with ≈2 : 1 and ≈1 : 1 H_2/CO compositions, which can be exploited respectively for the synthesis of methanol and aldehydes, with current densities >3.5 mA cm^{-2} in absolute value. Even if the medium-term stability of the cathodes under CO_2R conditions suffers from the partial leaching of the In-based active phase, their catalytic activity towards syngas formation can be restored upon further addition of the In(III) precursor to the electrolytic solution.

Future work will be directed towards the implementation of the proposed copper nanostructuring/indium functionalization electrochemical techniques to three dimensional substrates, such as Cu foams. The resulting cathodes would provide a porous environment with a highly exposed interfacial area, thus leading to higher currents. Furthermore, their use as gas diffusing electrodes can also be envisaged, in order to perform the reduction of CO_2 in the gas phase.

Conflicts of interest

The authors declare no conflict of interest.

Acknowledgements

This project received funding from the European Union's Horizon 2020 Research and Innovation Programme, under the Grant Agreement No. 101006839 (H2020 Research Innovation Actions 2020–2024 "CONDOR").

References

1 S. Nitopi, E. Bertheussen, S. B. Scott, X. Liu, A. K. Engstfeld, S. Horch, B. Seger, I. E. Stephens, K. Chan, C. Hahn, J. K. Nørskov, T. F. Jaramillo and I. Chorkendorff, *Chem. Rev.*, 2019, **119**, 7610–7672.
2 R.-P. Ye, J. Ding, W. Gong, M. D. Argyle, Q. Zhong, Y. Wang, C. K. Russell, Z. Xu, A. G. Russell and Q. Li, *Nat. Commun.*, 2019, **10**, 1–15.
3 A. M. Appel, J. E. Bercaw, A. B. Bocarsly, H. Dobbek, D. L. DuBois, M. Dupuis, J. G. Ferry, E. Fujita, R. Hille, P. J. Kenis, C. A. Kerfeld, R. H. Morris, C. H. F. Peden, A. R. Portis, S. W. Ragsdale, T. B. Rauchfuss, J. N. H. Reek, L. C. Seefeldt, R. K. Thauer and G. L. Waldrop, *Chem. Rev.*, 2013, **113**, 6621–6658.
4 C. Yang, Y. Wang, L. Qian, A. M. Al-Enizi, L. Zhang and G. Zheng, *ACS Appl. Energy Mater.*, 2021, **4**, 1034–1044.
5 A. Bagger, W. Ju, A. S. Varela, P. Strasser and J. Rossmeisl, *ChemPhysChem*, 2017, **18**, 3266–3273.
6 K. P. Kuhl, E. R. Cave, D. N. Abram and T. F. Jaramillo, *Energy Environ. Sci.*, 2012, **5**, 7050–7059.
7 C. W. Li and M. W. Kanan, *J. Am. Chem. Soc.*, 2012, **134**, 7231–7234.
8 H. Mistry, A. S. Varela, C. S. Bonifacio, I. Zegkinoglou, I. Sinev, Y.-W. Choi, K. Kisslinger, E. A. Stach, J. C. Yang, P. Strasser and B. Roldan Cuenya, *Nat. Commun.*, 2016, **7**, 1–9.
9 F. S. Roberts, K. P. Kuhl and A. Nilsson, *Angew. Chem.*, 2015, **127**, 5268–5271.
10 D. Gao, I. Zegkinoglou, N. J. Divins, F. Scholten, I. Sinev, P. Grosse and B. Roldan Cuenya, *ACS Nano*, 2017, **11**, 4825–4831.
11 M. E. Dry, *Appl. Catal., A*, 1996, **138**, 319–344.
12 M. E. Dry, *Catal. Today*, 2002, **71**, 227–241.
13 M. E. Dry, *J. Chem. Technol. Biotechnol.*, 2002, **77**, 43–50.
14 B. Kumar, J. P. Brian, V. Atla, S. Kumari, K. A. Bertram, R. T. White and J. M. Spurgeon, *ACS Catal.*, 2016, **6**, 4739–4745.
15 J. He, N. J. Johnson, A. Huang and C. P. Berlinguette, *ChemSusChem*, 2018, **11**, 48–57.
16 M. Carmo, D. L. Fritz, J. Mergel and D. Stolten, *Int. J. Hydrogen Energy*, 2013, **38**, 4901–4934.
17 A. Jedidi, S. Rasul, D. Masih, L. Cavallo and K. Takanabe, *J. Mater. Chem. A*, 2015, **3**, 19085–19092.
18 W. Luo, W. Xie, R. Mutschler, E. Oveisi, G. L. De Gregorio, R. Buonsanti and A. Züttel, *ACS Catal.*, 2018, **8**, 6571–6581.
19 Z. B. Hoffman, T. S. Gray, K. B. Moraveck, T. B. Gunnoe and G. Zangari, *ACS Catal.*, 2017, **7**, 5381–5390.
20 J. He, K. E. Dettelbach, D. A. Salvatore, T. Li and C. P. Berlinguette, *Angew. Chem.*, 2017, **129**, 6164–6168.
21 S. Rasul, D. H. Anjum, A. Jedidi, Y. Minenkov, L. Cavallo and K. Takanabe, *Angew. Chem.*, 2015, **127**, 2174–2178.
22 C. G. Vayenas, R. E. White and M. E. Gamboa-Aldeco, *Modern Aspects of Electrochemistry 42*, Springer Science & Business Media, 2008.
23 H. Kim, H. S. Park, Y. J. Hwang and B. K. Min, *J. Phys. Chem. C*, 2017, **121**, 22637–22643.
24 E. Irtem, T. Andreu, A. Parra, M. Hernández-Alonso, S. García-Rodríguez, J. Riesco-García, G. Penelas-Pérez and J. Morante, *J. Mater. Chem. A*, 2016, **4**, 13582–13588.
25 M. J. Siegfried and K.-S. Choi, *J. Am. Chem. Soc.*, 2006, **128**, 10356–10357.
26 M. J. Siegfried and K. S. Choi, *Adv. Mater.*, 2004, **16**, 1743–1746.
27 R. M. Arán-Ais, R. Rizo, P. Grosse, G. Algara-Siller, K. Dembélé, M. Plodinec, T. Lunkenbein, S. W. Chee and B. Roldan Cuenya, *Nat. Commun.*, 2020, **11**, 1–8.
28 C. Wagner, *Faraday Discuss. Chem. Soc.*, 1975, **60**, 291–300.
29 E. Bojestig, Y. Cao and L. Nyborg, *Surf. Interface Anal.*, 2020, **52**, 1104–1110.
30 I. Platzman, R. Brener, H. Haick and R. Tannenbaum, *J. Phys. Chem. C*, 2008, **112**, 1101–1108.
31 C. Yan, M. Zharnikov, A. Gölzhäuser and M. Grunze, *Langmuir*, 2000, **16**, 6208–6215.
32 Z. M. Detweiler, S. M. Wulfsberg, M. G. Frith, A. B. Bocarsly and S. L. Bernasek, *Surf. Sci.*, 2016, **648**, 188–195.
33 D. R. Baer and J. Moulder, *Surf. Sci. Spectra*, 1993, **2**, 1–7.
34 M. Brust, P. M. Blass and A. J. Bard, *Langmuir*, 1997, **13**, 5602–5607.
35 W. M. Skinner, C. A. Prestidge and R. S. C. Smart, *Surf. Interface Anal.*, 1996, **24**, 620–626.

36 R. Shiratsuchi, Y. Aikoh and G. Nogami, *J. Electrochem. Soc.*, 1993, **140**, 3479.
37 Y. Hori, A. Murata and R. Takahashi, *J. Chem. Soc., Faraday Trans. 1*, 1989, **85**, 2309–2326.
38 Y. Hori, A. Murata and Y. Yoshinami, *J. Chem. Soc., Faraday Trans.*, 1991, **87**, 125–128.
39 E. L. Clark and A. T. Bell, *J. Am. Chem. Soc.*, 2018, **140**, 7012–7020.
40 N. Gupta, M. Gattrell and B. MacDougall, *J. Appl. Electrochem.*, 2006, **36**, 161–172.
41 V. Dieterich, A. Buttler, A. Hanel, H. Spliethoff and S. Fendt, *Energy Environ. Sci.*, 2020, **13**, 3207–3252.
42 R. Franke, D. Selent and A. Börner, *Chem. Rev.*, 2012, **112**, 5675–5732.
43 G. n. O. Larrazábal, A. J. Martín, S. Mitchell, R. Hauert and J. Pérez-Ramírez, *ACS Catal.*, 2016, **6**, 6265–6274.